

Dynamics of enhanced gas trapping applied to CO₂ storage in the presence of oil using synchrotron X-ray micro tomography

Alessio Scanziani^{a,*}, Kamaljit Singh^b, Hannah Menke^b, Branko Bijeljic^a, Martin J. Blunt^a

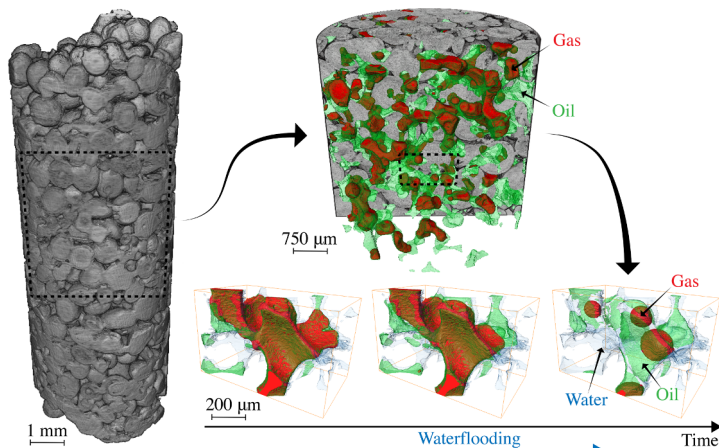
^a Department of Earth Science and Engineering, Imperial College London, SW7 2AZ, United Kingdom

^b Heriot-Watt University, Edinburgh, Scotland EH14 4AS, United Kingdom

HIGHLIGHTS

- We use fast synchrotron tomography to image three-phase flow in a porous rock.
- We capture the dynamics of displacement at micron resolution.
- Double and multiple displacement processes are observed.
- The presence of oil enhances gas trapping which helps safe storage.

GRAPHICAL ABSTRACT



ARTICLE INFO

Keywords:
CCUS
Three-phase flow
Capillary trapping
Multiple displacements
Gas storage
EOR
X-ray imaging
Synchrotron

ABSTRACT

During CO₂ storage in depleted oil fields, under immiscible conditions, CO₂ can be trapped in the pore space by capillary forces, providing safe storage over geological times - a phenomenon named capillary trapping. Synchrotron X-ray imaging was used to obtain dynamic three-dimensional images of the flow of the three phases involved in this process - brine, oil and gas (nitrogen) - at high pressure and temperature, inside the pore space of Ketton limestone. First, using continuous imaging of the porous medium during gas injection, performed after waterflooding, we observed chains of multiple displacements between the three phases, caused by the connectivity of the pore space. Then, brine was re-injected and double capillary trapping - gas trapping by oil and oil trapping by brine - was the dominant double displacement event. We computed pore occupancy, saturations, interfacial area, mean curvature and Euler characteristic to elucidate these double capillary trapping phenomena, which lead to a high residual gas saturation. Pore occupancy and saturation results show an enhancement of gas trapping in the presence of both oil and brine, which potentially makes CO₂ storage in depleted oil reservoirs attractive, combining safe storage with enhanced oil recovery through immiscible gas injection. Mean curvature measurements were used to assess the capillary pressures between fluid pairs during double

* Corresponding author.

E-mail address: alessio.scanziani16@imperial.ac.uk (A. Scanziani).

displacements and these confirmed the stability of the spreading oil layers observed, which facilitated double capillary trapping. Interfacial area and Euler characteristic increased, indicating lower oil and gas connectivity, due to the capillary trapping events.

1. Introduction

As the world looks for solutions to limit CO₂ emissions and mitigate climate change, carbon capture, utilisation and storage (CCUS) has been recognised as one of the key technologies to help prevent global warming [1–4]. Storage of CO₂ has been mainly studied in two types of underground formation: (i) saline aquifers and (ii) depleted hydrocarbon reservoirs [5,6]. When the CO₂ migrates in the subsurface, it can be trapped as pore-space bubbles in the rock. This process, known as capillary trapping, has been widely studied and can result in safe long-term storage. Several investigations have characterized capillary trapping in saline aquifers [4,7,8], while our work will focus on the trapping of CO₂ in oil reservoirs. We will study the pore-scale trapping of gas (representing CO₂ at immiscible conditions) in a depleted oilfield. The use of these fields for CO₂ storage can be economically advantageous, since the injected CO₂ can enhance oil recovery [9,10]. Furthermore, oilfields have retained hydrocarbons for geological time and so they are likely to provide good storage security for the injected CO₂ [11,2].

Capillary (or residual) CO₂ trapping is a key mechanism to secure CO₂ underground storage over thousands of years. In an immiscible system, the gas phase can be disconnected at the pore scale in the form of ganglia (or blobs), surrounded by other fluid phases and therefore trapped in the centres of pores. Due to immiscible conditions, the gas is unlikely to dissolve in oil and therefore these ganglia are immobilised forever by capillary and interfacial forces [5]. In the context of gas injection in oil reservoirs, the fluids responsible for capillary trapping are brine and oil, both already present in the pore space of the rocks, hence resulting in three-phase flow when gas is injected.

At the field scale, Qi et al. developed a model for predicting the amount of CO₂ trapped in aquifers [12] and oilfields [13]. These studies demonstrated that a chase brine injection which followed gas injection can trap most of the gas in the reservoir, due to capillary trapping. However, the amount of trapped gas (residual gas saturation) is very sensitive to the choice of the trapping model built on smaller scale experiments.

Data from experiments on cm-sized rock samples (cores) can be used to develop empirical models for trapping. The most widely used of these was proposed for two-phase systems by Land [14] and relates the final amount of gas trapped (residual gas saturation S_{gr}) with its initial saturation S_{gi} through the trapping constant C:

$$S_{gr} = \frac{S_{gi}}{(1 + CS_{gi})}. \quad (1)$$

For three-phase flow, however, the physics are complicated by the fact that both oil and brine may contribute to trapping.

Amaechi et al. [15] studied trapping for three-phase flow in sand-packs, and showed that the trapping of gas could be larger in the presence of both oil and water, with respect to two-phase experiments where gas was trapped by either just oil or water. They suggested that the presence of spreading oil layers helped enhance gas trapping, but did not image the pore-scale distributions of fluids. Scanziani et al. [16] performed three-phase flow experiments, with static imaging, and confirmed that oil layers enhance the trapping because gas is strongly non-wetting to oil (the effective contact angle is zero). We aim to investigate these trapping phenomena further using fast synchrotron imaging to elucidate the dynamics of trapping at the pore-scale.

The formation of oil layers is thermodynamically regulated by the spreading coefficient (C_s), which derives from a force balance involving

interfacial tensions σ_{ij} , where g is gas, w water and o oil [5]:

$$C_s = \sigma_{gw} - \sigma_{ow} - \sigma_{go}. \quad (2)$$

The oil phase spreads in a layer between water and gas if the spreading coefficient is positive or close to zero. If the spreading coefficient is strongly negative, the formation of oil layers is not favoured. [17]

One unique feature of three-phase flow is double displacement, where one phase displaces a second which displaces the third, even under conditions of capillary equilibrium [18]. Furthermore, it is possible to have multiple displacements, where one phase displaces another, which displaces another and so on, with any number of intermediate steps [19]. Previous studies of three-phase flow in micromodels showed the occurrence of double [20,18] and multiple displacement events [21,20]. For instance, Sohrabi et al. [20] observed double displacement events (gas displacing oil displacing water) with the first gas injection, and multiple displacements (where the displaced oil and water further mobilize other fluids) with subsequent water-alternating-gas (WAG) injections. Gas displacing oil displacing water is usually called double drainage and it allows for further oil recovery, as observed in other micromodel studies [18]. When brine displaces oil which displaces gas, the process is named double imbibition. This has also been observed in micromodels [22,23], and can enhance gas trapping.

However, the micromodels used for previous three-phase flow studies were two-dimensional (2D) lattices, while real pore systems are three-dimensional (3D). These 3D pore systems tend to have more complex geometries with higher pore space connectivity and thus there is an increased potential for double and multiple displacement cascades.

X-ray micro-computed tomography (μ CT) provides 3D *in situ* images of the pore space, and has recently revolutionised research in flow in porous media [24,25,5,26]. Several studies have visualized capillary trapping of gas during water injection in two-phase flow [27–31] while only a few have considered trapping in three-phase flow [32,33,16].

The presence of double displacement events in 3D was inferred by Scanziani et al. [16] in a water-wet medium for immiscible conditions, by Alhosani et al. [34] at miscible conditions and by Qin et al. [35] in weakly oil-wet media, from static end-state images. To directly observe these events, and investigate the presence of multiple chains of displacement, in this work we used synchrotron-based X-ray imaging, which captures the dynamics at the pore scale during a displacement [36–41]. First, we dynamically imaged the occurrence of both double and multiple displacements during gas injection in the 3D pore space of a Kettom limestone saturated with brine and oil. We then performed injection of chase brine to increase gas trapping [13,12]. To this end we seek to elucidate the mechanisms responsible for additional trapping. For single displacements in two-phase flow, during imbibition there is a competition between piston-like displacement and snap-off, i.e. the trapping of the non-wetting phase due to the swelling of the wetting phase [5,38]. This holds also for multiple displacements. In water-wet systems, double imbibition is likely to favour snap-off over piston-like displacement and the double mechanism becomes a double capillary trapping event - gas trapping by oil and oil trapping by water. This has ultimately a strong impact on the final amount of trapped gas.

In this work, we will show how the presence of spreading oil enhances the capillary trapping of gas, as gas is strongly non-wetting to oil [15], through double capillary trapping events. We will use quantitative measures such as saturation, interfacial area, the mean interfacial curvature and the total interfacial curvature, related to the Minkowski functionals [42,43], to describe how brine and oil trap the gas in the

centre of the pores during the chase water injection.

Using fast synchrotron imaging of a porous rock at high pressure and temperature, we will provide (i) direct visualisation of multiple displacement during gas injection and (ii) a quantification of double capillary trapping events, which dominate during the following brine injection and enhance gas trapping in hydrocarbon reservoirs.

2. Materials and methods

We used dynamic imaging at the I13 beamline of the Diamond Lightsource synchrotron facility (Harwell Campus, Didcot, Oxfordshire) to obtain information about the evolution of the arrangement of the phases in the pore space over time, to complement the experiments previously performed in laboratory-based X-ray μ CT [16]. In our case, each scan was acquired in 32 s, with an offset time of 20 s, resulting in a dataset of 867 tomograms collected every 52 s over the course of 12.5 h. The experiment was performed similarly to the one described in [16], with some differences in the mass percentage of dopants used, due to the difference in the X-ray beam type, and flow rates, which have been slowed down to capture a sequence of pore-scale displacements.

2.1. Materials

The experiment was performed using a sample of Ketton carbonate (Ketton, Rutland, UK), with a diameter of 3.8 mm and length of 8.8 mm, drilled from a bigger core, as shown in Fig. 1. The composition of the rock is > 99% calcite [28] and porosity was measured to be 28.7% with a Helium porosimeter and 16.4% with image analysis, which only captured the larger pores which can be seen in the scans. The micro-porosity is hence 12.3%. Micro pores are defined as those which cannot be resolved at a voxel size of 3.58 μ m, and this definition agrees with the dual pore-size distribution provided by [44]. This micro-porosity remained water-saturated during the experiment and therefore will increase water connectivity above that apparent in the macro-pore space [45]. The increase in connectivity can favour multiple displacements and capillary trapping, but does not change the overall picture of these phenomena. Brine was a mixture of 25% by weight KI in water and oil was a mixture of 20% by weight iododecane in n-decane. The gas phase was pure nitrogen. We used nitrogen for this first synchrotron study of three-phase flow not to over complicate the system with miscibility or reaction issues that would have occurred with the use of non-equilibrated CO_2 . As shown by Niu et al. [46], CO_2 and nitrogen have almost identical trapping curves. The results of our study are then applicable to those cases where an immiscible gas (e.g. CO_2 , nitrogen or methane at immiscible conditions) is injected in porous media in the

Table 1

Thermophysical properties of the selected phases. Density and viscosity are computed from experimental conditions (8 MPa and 60°C) data of pure elements provided in [60]. Interfacial tensions are measured at 1.01 MPa and 298.15 K.

	Density [kg/m ³]	Viscosity [μ Pa × s]	Interfacial tension [mN/m]
Brine ($\text{H}_2\text{O} + 25\%$ w KI)	1052	1237	$\sigma_{ow} = 47 \pm 4$
Oil (Decane + 20%w Iododecane)	931.7	1752	$\sigma_{go} = 27 \pm 4$
Gas (N_2)	93.78	19.01	$\sigma_{gw} = 72 \pm 5$

presence of oil and water. The thermophysical properties of the phases are shown in Table 1. The amount of dopants used was determined using a preliminary study of attenuation coefficients with X-ray energy [16] and allowed for good contrast between the four phases: nitrogen, oil, brine and rock in brightness order as illustrated in Fig. 2A. Further details on the imaging are provided in the Supplementary Material.

The sample was prepared and placed in a core holder as described in [47,48,29], and 5 pumps (Teledyne ISCO, Lincoln, NE, USA) were used to maintain the pressure and inject the fluids in the sample with the method described in Scanziani et al. [16]. A heating jacket was wrapped on the carbon fibre Hassler type flow cell and a thermocouple was placed next to the rock. A proportional-integral-derivative (PID) controller was connected to both the jacket and the thermocouple which ensured that the temperature was kept constant during the experiment. Experimental conditions were 8 MPa pressure and 60°C at the sample location. A confining pressure of 10 MPa was kept in the annulus between the core holder and the sleeve wrapping the sample to prevent bypassing of the fluids along the sides. Aluminium tape was placed around the sleeve to avoid diffusion of the gas through the sleeve.

2.2. Injection sequence and imaging

The sample was first flushed with CO_2 to remove air and then fully saturated with brine at a flow rate of 0.1 mL/min for 20 min. Oil injection (OI) was performed at 0.01 mL/min from the top of the sample for a total of 20 pore volumes injected (PVI). A pore volume was computed using the volume of the whole sample and accounting for its total porosity. Imbibition was then performed by injecting brine from the bottom of the sample, at 0.01 mL/min, for a total of 5 PVI (first waterflooding, WF1). To capture three-phase flow dynamics, subsequent gas injection (GI) was performed at a lower flow rate

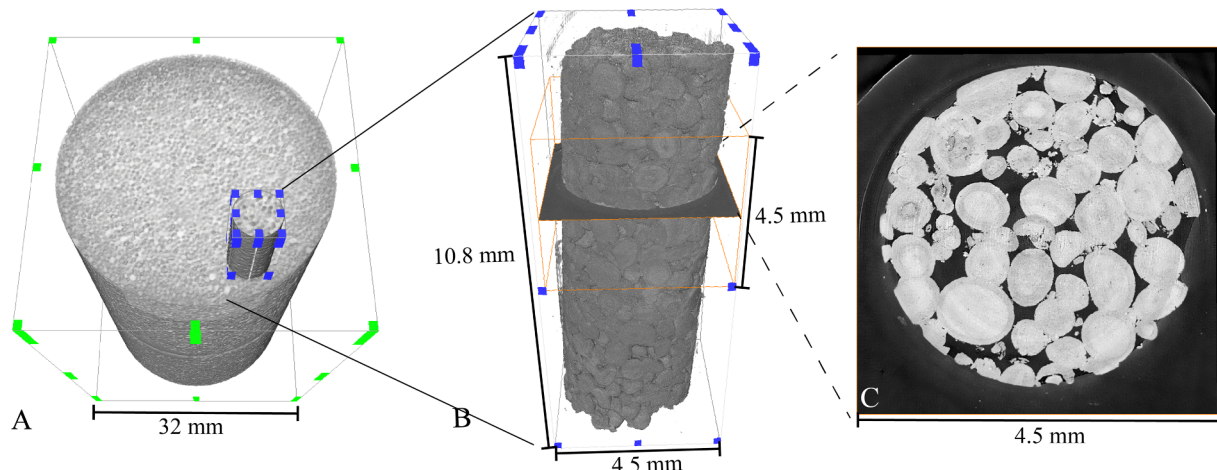


Fig. 1. A homogeneous location was selected from a core plug with diameter of 3.1 cm (A), and a core with 3.8 mm diameter was obtained (B). The scan location is indicated by the orange box in B. Panel C shows a slice of the dry scan of the rock.

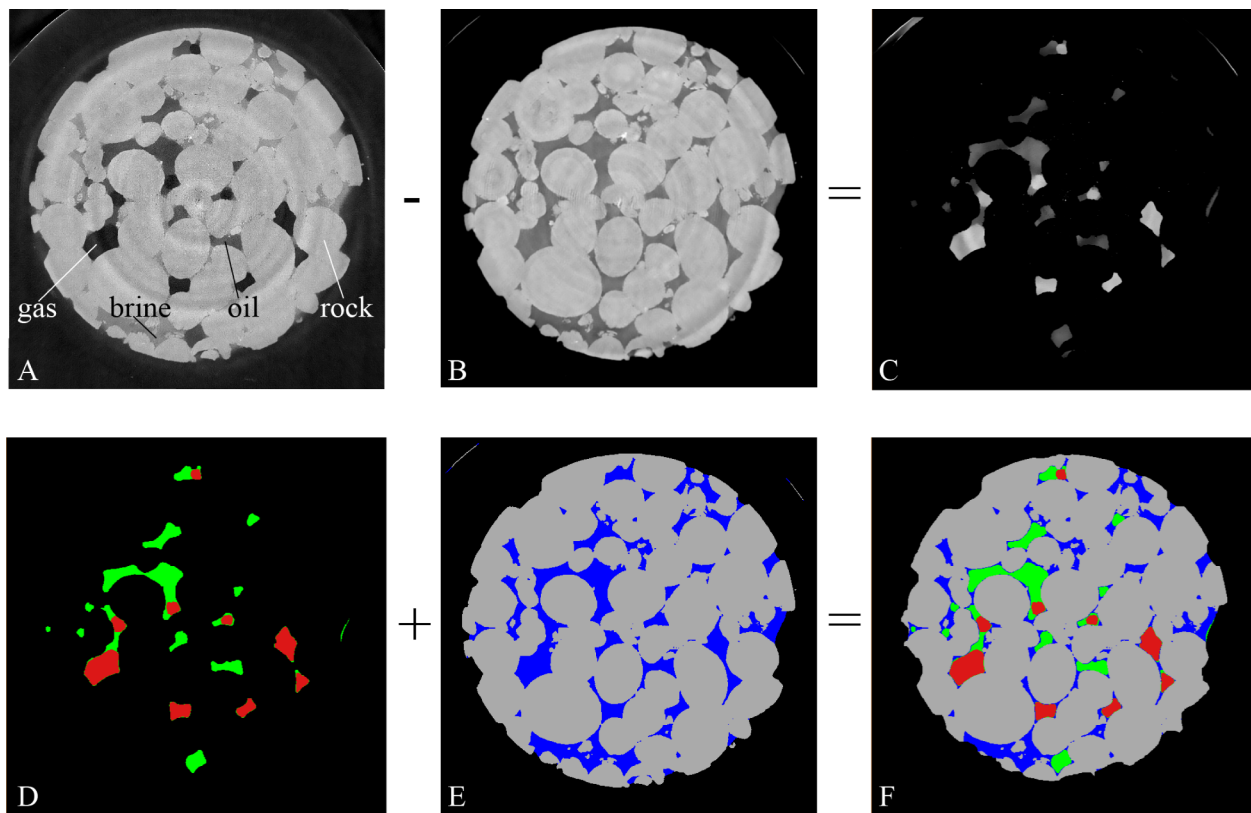


Fig. 2. A: slice of a 3D image with the presence of all the phases (gas, oil, brine and rock from the darkest to the brighter phase), after the first non-local-means filtering step. We subtracted image A to the brine filtered image (B) to obtain only oil and gas (C). From C, we were able to obtain oil (green) and gas (red) with simple thresholding segmentation (D). Adding the dry image (E) to D, we obtain the final image F with all the four segmented phases (brine is blue and rock is grey).

(0.0004 mL/min) for a total of 6.12 PVI and the second waterflooding (WF2) was performed at 0.0001 mL/min for a total of 4.2 PVI. The sample was continuously imaged during each of the injections, using an objective with a 2x lens, ensuring a voxel size of 3.58 μm , with a 4.3³ mm³ cubic field of view located at the middle-top part of the sample as shown in Fig. 1.

2.3. Sample initialization

Starting with 100% brine saturation, the oil saturation increased during OI and then stabilised around a value of 55%, with no further major change of saturation over time. During WF1, the oil saturation decreased as the invading brine pushed some oil out of the sample. This happened within a time frame of about 10 min with a flow rate of 0.01 mL/min, which corresponds to approximately 5 pore volumes (PV). However, not all the oil in place could be produced, and a considerable amount of oil remained trapped in the pore space and could not be displaced with further brine injection, due to capillary trapping or bypass, as observed in previous studies [29,38]. In our case, the saturation of oil at the end of WF1 was close to 50%. The saturations were defined based on the fraction of the resolvable, macro-pore space occupied by each phase; we did not consider micro-porosity.

2.4. Image analysis

All the tomograms were reconstructed, and 3D grey-scale images were obtained (Fig. 2A). However, to obtain quantitative information from the images, a segmentation step is needed, consisting of the assignment of each voxel to the phase at a particular location. In our study, we need to classify the voxels into four groups (or materials): gas, brine, oil and rock. The different attenuation coefficients of the four materials (thanks to the use of the dopants), gave them distinct grey-

scale values, as seen in Fig. 2A. An automatic segmentation procedure has been developed and applied to all the tomograms, as described below. (i) First, the multiphase image was filtered with a non-local-means filter (NLMF, Fig. 2A) to remove noise [49]. (ii) Then, we subtracted the three-phase image from the brine saturated image (Fig. 2B). This was done to take the rock and brine voxels out of the image, and only oil and gas were left. The resulting image was filtered again with a NLMF (Fig. 2C). (iii) Oil and gas phases were segmented applying grey-scale value thresholds to the images obtained from the previous step (Fig. 2D). (iv) The dry scan was used to add the rock phase, as our experiment did not alter the shape of the grains (Fig. 2E), and the remaining voxels were assigned to brine (Fig. 2F).

Once the segmented images were obtained, we used image analysis techniques to quantify saturation, connectivity, thickness, curvature, interfacial area and Euler characteristic.

2.4.1. Minkowski functionals

Minkowski functionals are morphological functions which can be computed from binary 3D images and relate mechanical and hydraulic characteristics with the 3D topology of the pore space [50]. For a 3D image, 4 Minkowski functionals are defined: the zeroth-order is volume of the pore space. In multiphase flow, this can be defined as the volume of each phase, which is proportional to the saturation.

The first-order functional is the interfacial area. We measured the interfacial areas between brine and oil, and between oil and gas. The interfacial area between gas and water was not computed as the presence of oil layers prevents their direct contact.

The average curvature of the interfaces between two phases κ_{ij} is the second-order Minkowski functional. κ_{ij} can be related to the capillary pressure $P_{c,ij}$ between the two phases through the interfacial tension at the interface with the Young-Laplace equation:

$$\kappa_{ij} = 2\sigma_{ij}\kappa_{ij}, \quad (3)$$

where the fluids i and j will be respectively oil (o) and water (w) or gas (g) and oil. Hence $\kappa_{ow} > 0$ when $P_{c,ow} > 0$ ($P_o > P_w$) and $\kappa_{go} > 0$ when $P_{c,go} > 0$ ($P_g > P_o$). We will use Eq. (3) to relate κ_{ij} with multiple displacements.

κ_{ij} can be also geometrically linked to the thickness of oil layers: the larger the difference between oil/brine and gas/oil curvature, the thicker the oil layer. In contrast, if the two curvatures are similar, the oil layers become thinner and less stable until they collapse.

The total curvature of the interface, the third-order Minkowski functional, has a less immediate relation with a physical property. However, Vogel et al. [43] showed that it is directly linked to the Euler characteristic of a 3D object, χ . This topological descriptor, if generalised using the three Betti numbers β_0 , β_1 and β_2 , can be used to describe the connectivity of the pore space [5]:

$$\chi = \beta_0 - \beta_1 + \beta_2. \quad (4)$$

These three numbers are defined as the number of discrete disconnected objects in the pore space (β_0), the number of loops in its structure (β_1) and the number of isolated voids or holes in the 3D volume (β_2). The most non-wetting phase (gas in our case), does not have holes in its volume ($\beta_2 = 0$) and usually has a limited number of loops. For this reason, the Euler characteristic provides a quantitative measure of gas connectivity.

2.4.2. Saturation, connectivity and thickness

The saturation of the three phases was computed by dividing the number of voxels assigned to a phase by the total number of voxels comprising the pore space. Connectivity analysis consisted of considering one phase at a time and identifying and labelling its disconnected clusters.

The thickness of a phase was computed by fitting maximum balls in the 3D region assigned to the selected phase and the diameter of each sphere defined the local thickness [51].

2.4.3. Interfacial area, curvature and Euler characteristic

Fluid/fluid interfaces were identified and a marching cubes algorithm was used to extract a 3D triangular mesh. This algorithm includes a smoothing step, to remove voxelization artefacts. The size of the filter kernel and thus the extent of smoothing applied to the surface, was set at 5 voxels. The specific interfacial area is the area of these interfaces divided by the total volume.

For computing curvature some further steps were required: (i) One smoothed interface was selected (gas/oil or oil/brine); (ii) the curvature of the interface was computed by fitting locally a quadratic form to the smoothed surface; (iii) a distance map of the pore space was computed from the dry images and (iv) the values of curvature were filtered selecting and discarding the ones computed in the locations close to the walls of the grains (distance < 3 voxels), using the distance map previously computed. This was done due to the lower quality of the images in these locations. Further information about curvature measurements can be found in [52]. All the calculations were performed using commercial image analysis software (Thermostisher Avizo 9.5).

The specific Euler characteristic was computed from the binary segmented images of gas and oil using the MATLAB script developed in [53] and normalised with the total volume of the image.

2.4.4. Contact angle

The wettability of the system was quantified through direct measurement of *in situ* contact angles. We used an automatic method developed by Scanziani et al. [47], which first finds the contact line (the set of the fluid/fluid/solid contact points) from 3D images. Then, it uses this line to find the 2D slices of the 3D images of the sample saturated with fluids where the main radius of curvature is defined. The effective contact angle is computed on these 2D slices by using the constant

curvature constraint provided by the Young-Laplace equation, Eq. (3), to fit a circle to the fluid/fluid interface and a line to the solid surface. The angle between the tangent to the circle at the contact point and the line representing the solid surface is the contact angle at the location considered.

2.4.5. Pore occupancy

We used the maximal ball method included in the generalized network extraction algorithm developed by Raeini et al. [54] to extract a set of spheres representing the pores inside the sample. Their diameter was used as a proxy for pore dimension. We then used grey-scale images to identify the phase which occupies the space identified by each sphere, thus assigning each pore (with its dimension) to one of the three phases. This allows us to obtain a relationship between a pore's dimension and the phase at its centre, which then determines pore occupancy [16,55,16].

3. Results and discussion

First (Section 3.1), we injected gas and we observed the formation of oil layers and the appearance of both double and multiple displacements. These caused changes in both the saturations of the phases - with improved oil recovery - and their arrangement in the pore space. Although the dominant displacements observed were of drainage type, we also noticed local imbibition-type mechanisms.

Second (Section 3.2), brine was re-injected in the sample. Double imbibition was the dominant double displacement observed. In particular, double capillary trapping dominated over double piston-like displacement, leading to a large amount of gas trapping. We used image analysis techniques to obtain topological measures related to the Minkowski functionals and quantify the double capillary trapping events.

Last, in Section 3.3, we explain why gas trapping is favoured in the presence of both oil and gas, using measures of wettability.

3.1. Gas injection (GI)

Gas injection was performed at a flow rate of 0.0004 mL/min, corresponding to a capillary number of 2×10^{-11} . Since gas is the most non-wetting phase, it invaded the centre of the larger pores, as highlighted in [16] with a pore occupancy analysis. Water, in contrast, is confined to the smaller pores and the corners and roughness of gas-occupied elements. The spreading coefficient of the oil phase is -2 mN/m, using the values in Table 1 and Eq. (2) [5]. Although the value is negative, its magnitude is small which means that stable oil layers can form in the pore space sandwiched between gas in the centre and water in the corners, as observed previously with pore-scale imaging [16]. Hence, when gas is injected, previously disconnected oil reconnects in layers.

The saturation of the phases during GI experienced fluctuations over time, even after several minutes, as shown in Fig. 3. This was caused by dynamic rearrangement of the phases due to cascades of multiple displacements, described in the next section. We also observed drainage of oil layers and an overall decrease of oil saturation, while the gas saturation increased as it was injected into the sample. This process was slow and continued until 6.12 pore volumes of gas were injected (Fig. 3).

Fig. 4 illustrates how the connectivity of oil and gas changed during GI. Gas re-arranged in the pore space during the injection with local trapping and disconnection by oil and water, while oil always remained connected through layers. At the end of GI, the oil and gas saturations were 19% and 40% respectively, with 47% oil recovery with respect to the oil saturation at the beginning of gas injection (time 0 in Fig. 3).

3.1.1. Dynamics of gas injection and multiple displacements

With dynamic imaging of gas injection we observed how the gas phase invaded the pore space in the presence of oil and brine. The top

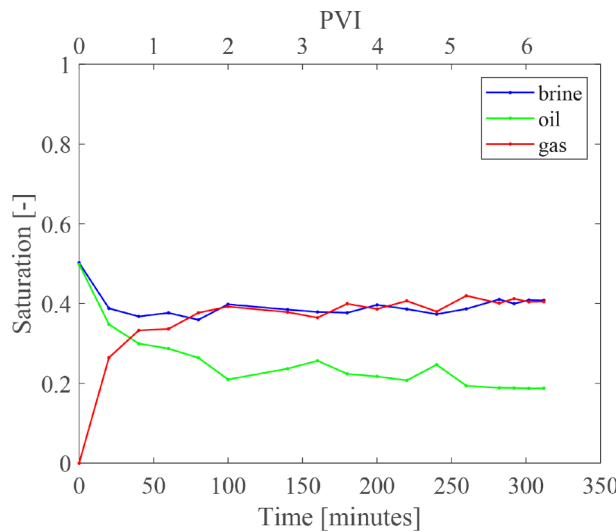


Fig. 3. Saturation of brine, oil and gas over time during GI. Time = 0 at the beginning of gas injection and PVI = pore volumes injected since GI started.

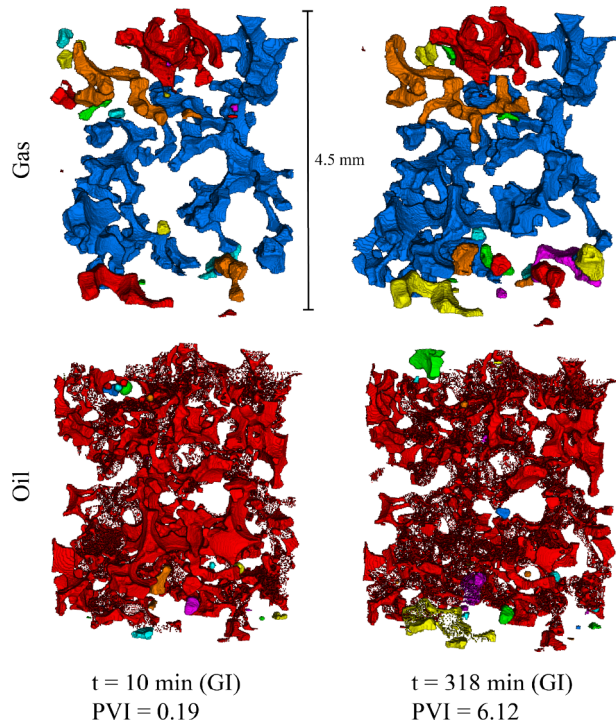


Fig. 4. Connectivity of gas and oil during GI. Different colours indicate different clusters. The top row represents gas only and the bottom row oil only. The gas phase was distributed in a main connected cluster and smaller disconnected ones, with an overall rearrangement over time as its saturation increases (top right). The oil phase remained connected in oil layers through the whole domain from the beginning to the end of GI. PVI = pore volumes injected since GI started.

part of Fig. 4 shows that the arrangement of gas in the pore space varied with time. Even if we can observe a cluster of gas connected through the imaged volume, 3D connectivity shows that we have dynamic rearrangements, causing an evolution of the shape and number of gas ganglia. These events occurred between two subsequent scans, 52 s apart. This has also consequences on the saturations of the three phases, which show fluctuations during time (Fig. 3). This dynamic connectivity of the flowing phase has also been previously observed during steady-state two-phase flow [40,56,57]. However, the driving force for

non-wetting phase dynamics is thought to be viscous effects [40]; in this case the extremely low capillary numbers imply that this dynamics occurs even under capillary-controlled conditions as the result of the flow of three phases [5,18]. Although an energy balance can be performed to assess the ability for these displacements to occur [40], we suggest that here they represent capillary-controlled events which lower the interfacial energy. Double and multiple displacements were responsible for dynamic connection and disconnection of gas as its saturation globally increased, until equilibrium was reached when we had injected about 5 pore volumes and then less movement was observed.

Fig. 5 shows different 3D time frames of a subvolume of the pore-space where gas is shown in grey and oil was rendered as a colourmap according to its thickness.

Gas is at first disconnected by oil (Fig. 5 at minute 240), due to either distal or Roof snap-off, as previously observed in two-phase drainage displacements [28,57]. Later, we observe multiple displacements, where one phase displaces another that can displace another in a chain of events of arbitrary length [58]. Overall we see a double drainage process [18] where gas displaces oil that displaces water. However, as shown next, this is often accompanied by imbibition processes where the water displaces oil which displaces (and can trap) gas.

At minute 271 gas, previously disconnected, is reconnected in the throat highlighted with a triangle in Fig. 5. The circled region, instead, experienced different types of double and multiple displacements. Firstly, between minutes 240 and 271, a double displacement mechanism (double drainage, DD) was observed, with the invading gas displacing oil which displaces water, in the presence of a thin oil layer (their mean thickness is approximately 10 μm). Later, some oil was provided in the region from other parts of the pore space through the connected layers. This caused a local multiple displacement, and particularly an imbibition-drainage-drainage (IDD), where oil displaced gas (imbibition, I) which displaced the oil layer (drainage, D) which in turn displaced water (drainage). The displaced water is connected on the surfaces of the grains and later caused, in the same throat, as a chain, a local double imbibition (specifically imbibition-imbibition-drainage-drainage IIID) in the form of double capillary trapping. As a consequence of this latest event, gas remained trapped in the pore surrounded by oil layers. This double imbibition process was noticed to be dominant in the subsequent brine injection, described in the next section.

We have just described how, during the first gas injection, in the presence of oil and brine, both double and multiple displacement happened. This is in contrast with what was previously observed in 2D micromodels, where multiple displacements were observed only in later WAG cycles [20,21], and in our case is enabled by the increased connectivity provided by the 3D structure of the pore space. In the sub-volume of Fig. 5 we have identified one double displacement and two multiple displacement events. We expect that in a bigger region of the rock multiple displacements are more frequent and dominate the rearrangements and changes in connectivity during three-phase flow.

3.2. Second waterflooding (WF2) and double capillary trapping

After gas injection, we re-injected brine in the sample (second waterflooding, WF2). This injection is particularly useful for gas storage purposes, as the previously injected gas can be trapped [12,13,16]. The difference from two-phase capillary trapping is that in three-phase flow we also have the presence of oil layers sandwiched between gas and brine phases and the trapping is caused by double imbibition displacements - brine displacing oil displacing gas.

The behaviour of oil and gas during WF2 is shown in Fig. 6, which illustrates their connectivity with different colours associated to disconnected ganglia. To fully investigate the double capillary trapping of oil and gas, we will study the evolution of the Minkowski functionals over time. Specifically in Fig. 8 we plot the saturation, number of ganglia per unit volume ($1/\text{mm}^3$), average ganglion volume, and Euler

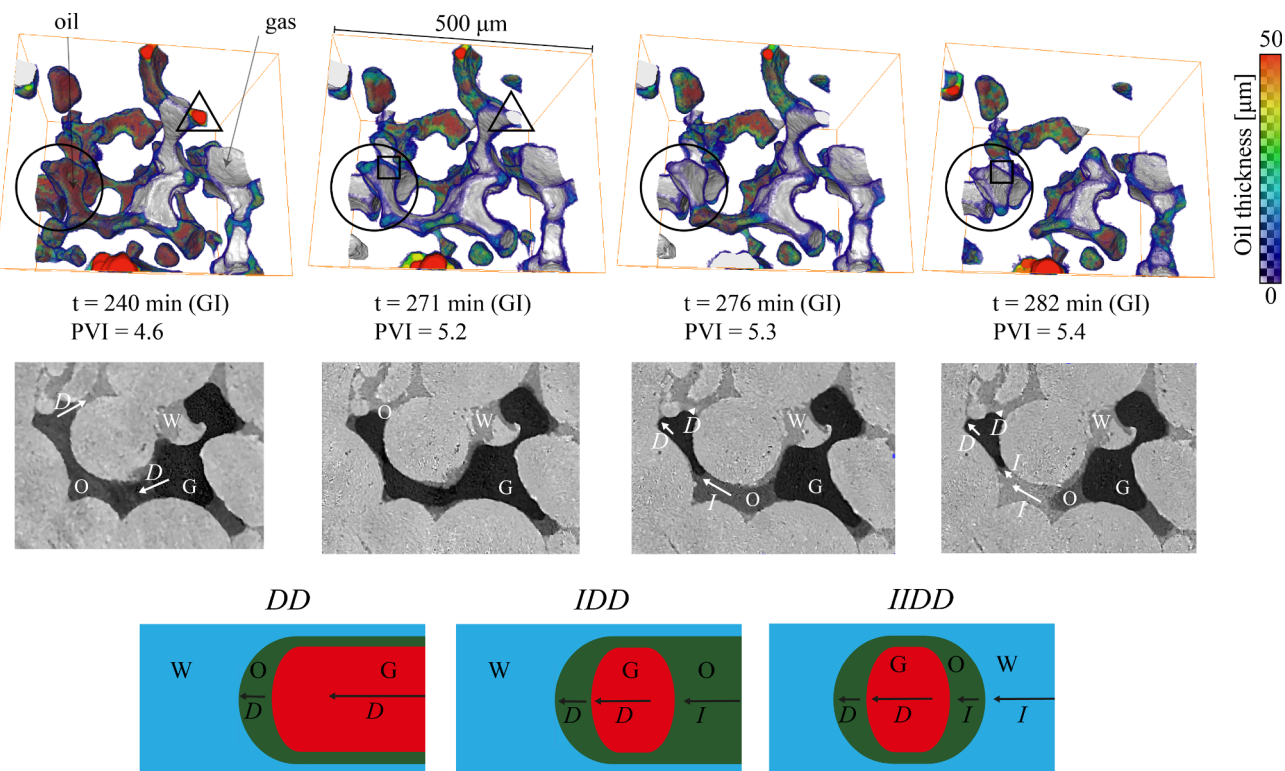


Fig. 5. On top: three-dimensional rendering of gas (in grey) and oil phases in a subvolume during gas injection, at different time steps. The oil phase is coloured based on its thickness, computed fitting maximum balls in the region of the space segmented as oil phase [51]. The overall flow is from the top to the bottom of the images. In the middle row we show the grey scale images, sectioning the 3D image in top row at the circled location, highlighting the drainage (D) and imbibition (I) displacements and the three phases (water W, gas G and oil O). In the bottom part of the figure, we illustrate a schematic of the three double displacement mechanisms recognised in the circled throat and in the middle row, using a representation introduced by Keller et al. [22] for micromodels. D stands for drainage and I for imbibition. PVI = pore volumes injected since GI started.

characteristic as a function of time for both oil and gas. We also show the interfacial areas and curvatures for gas/oil and oil/brine menisci. We started counting the time associated to WF2 as soon as we started injecting brine into the inlet flow lines. However, the actual invasion of brine in the imaged portion of the core happened several minutes later, as first the brine had to cover the dead volumes of the flow loop and invade the bottom part of the sample, which was not continuously imaged (Fig. 1). Hence, until minute 198, we observed effectively further gas injection with a corresponding increase in gas saturation to around 45%, while the first changes associated with water invasion were observed in the domain from minute 199.

3.2.1. Oil trapping gas

Between minutes 199 and 202 (Fig. 6), we observe that the invading brine displaced some oil from the bottom part of the sample (below the field of view), with a local increase in oil saturation in the imaged domain (Fig. 7A). The gas saturation decreased, again due to displacement by brine. The number of oil ganglia remained constant, while their volume increased (Fig. 7C), meaning that the layers of oil swelled. This swelling of oil layers caused some gas ganglia to be trapped in the centre of the pores (Fig. 6E), with an increase in the number of gas ganglia and a decrease of their mean volume (Fig. 7D). Due to the local increase in oil saturation and the gas-trapping-by-oil events, the oil/brine and gas/oil interfacial areas increased (Fig. 7B).

3.2.2. Double capillary trapping events

In the next tomograms, we observed how the injected brine caused double capillary trapping events: brine layers swelled, pushing on the interface between brine and oil. Some oil was then initially produced, as it was still mostly connected in layers through the sample (Fig. 6H), leading to a decrease in oil saturation shown in Fig. 7A between

minutes 202 and 205. At some point, however, the swelling of brine layers caused the disconnection of oil, and we observe a rapid increase in the number of oil ganglia and a decrease in their mean volume at minute 206 (Fig. 7C), with a sudden increase in oil/brine interfacial area. During this process, the oil phase was also moved towards the centre of the pores, pushed by brine. This movement of the oil phase affected the gas, which was in direct contact with oil through oil/gas interfaces. First, some gas was pushed out of the sample and produced, through its dynamic connectivity (previously described in Section 3.1.1), decreasing its saturation in the domain. Most of the gas (about 66%), however, was snapped-off by oil and capillary trapped in the centre of the pores, associated with an increase in gas/oil interfacial area (Fig. 7B).

Mean curvature. The Young-Laplace equation, Eq. (3), directly relates the mean curvature between two phases with their capillary pressure. Looking at Fig. 7E, we see that during gas injection (solid line), when the dominant double displacement mechanism was double drainage, the curvatures between gas and oil (κ_{go}) and oil and brine (κ_{ow}) are higher than during the double imbibition displacements (dashed lines). The local capillary pressures during double drainage (DD) are higher than during double imbibition (II), as in a DD mechanism gas displaces oil (and hence needs higher pressure with respect to oil) and oil displaces brine. In an II mechanism, instead, brine displaces oil and oil displaces gas, lowering the capillary pressures. In symbols:

$$P_{c,ij,DD} = (P_i - P_j)_{DD} > P_{c,ij,II} = (P_i - P_j)_{II}, \quad (5)$$

with $i, j = g, o$ or w . Using Eq. (3) we can rewrite Eq. (5) in terms of curvatures:

$$\kappa_{ij,DD} > \kappa_{ij,II}. \quad (6)$$

The curvatures are plotted in Fig. 7E.

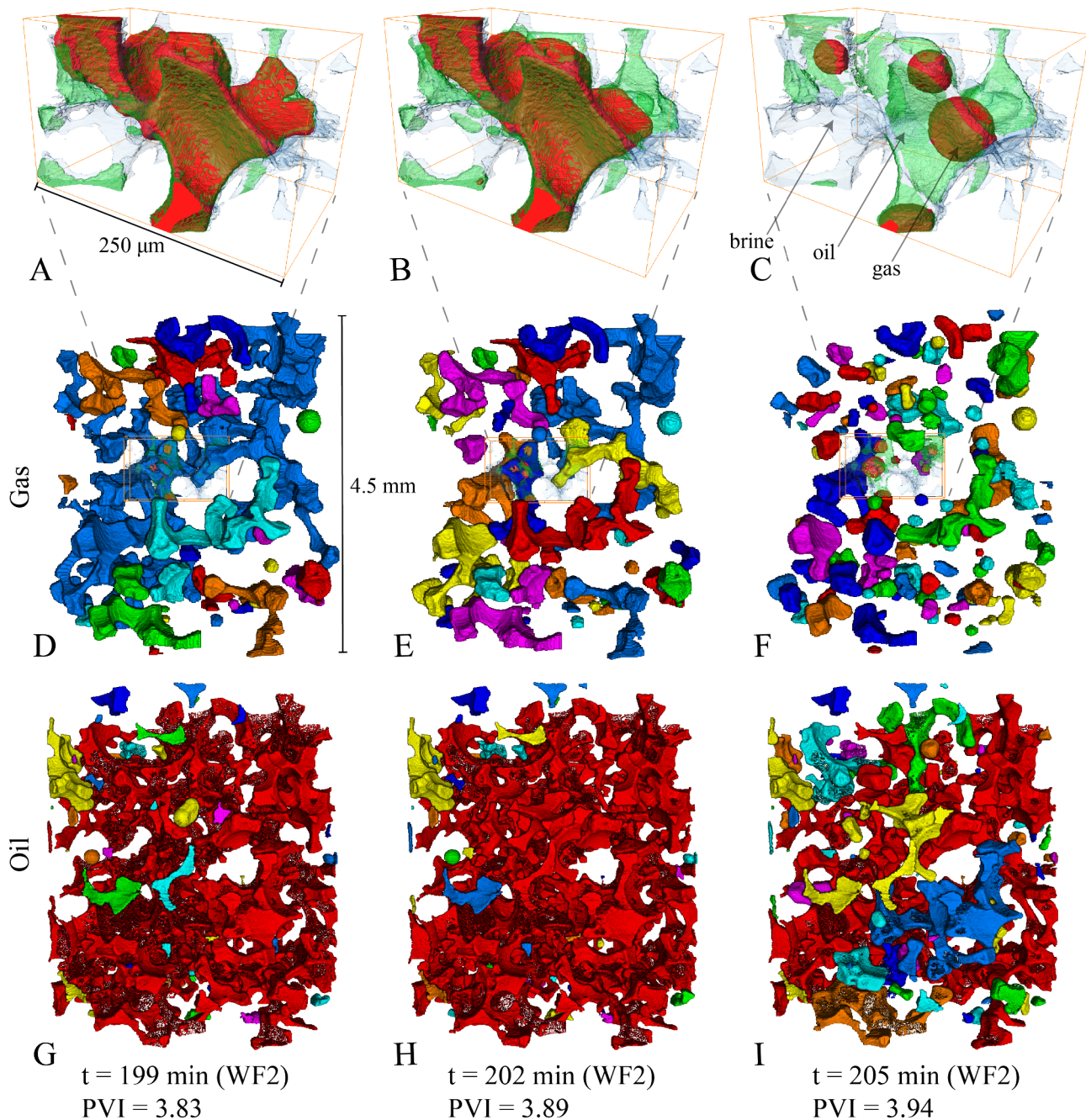


Fig. 6. 3D rendering of the phases during WF2. A-C show a subvolume where brine (transparent blue), oil (green) and gas (red) were imaged at three time steps: just before ($t = 199$), during ($t = 202$) and after ($t = 215$) the double capillary trapping events. D-F show the connectivity of gas phase only and G-I the connectivity of oil phase only for the full dynamically imaged domain at the same time steps. For panels D-I, different colours represent distinct ganglia. PVI = pore volumes injected since WF2 started.

The difference in the values of mean curvature can also be related to the thickness of the oil layer. Indeed, oil layers will be thicker when the difference between κ_{ow} and κ_{go} is higher (refer to the sketch in Fig. 7E). Hence, during double drainage, oil layers will be thicker than during double imbibition. This was measured for the region highlighted with a square in Fig. 5: the local thickness of oil layers during double drainage (minute 271 of GI) was measured to be $14 \pm 5 \mu\text{m}$ while during double imbibition (minute 282) it was $7 \pm 5 \mu\text{m}$. Oil layers would collapse and disappear when $\kappa_{ow} = \kappa_{go}$, and this never occurred, meaning that gas was always surrounded by oil layers.

Euler characteristic. The gas phase specific Euler characteristic (in red in Fig. 7F) can be interpreted considering the definition of Euler characteristic using the Betti numbers, Eq. (4). Gas was the most non-

wetting phase and occupied the centre of the bigger pores [16]. Thus, its 3D volume does not have internal voids ($\beta_2 = 0$) and a limited number of loops ($\beta_1 \ll \beta_0$), hence the gas specific Euler characteristic is positive and follows the number of gas ganglia (in light red in Fig. 7D), with a sudden increase as the gas was trapped between minutes 200 and 205.

The oil phase specific Euler characteristic (in green in Fig. 7F) is lower, as oil was present in connected layers. During gas injection (solid line), the oil topology was characterized by many loops (β_1) and internal voids (β_2), occupied by the injected gas phase. The number of these loops and voids changed rapidly during the displacement as the fluids rearranged in the pore space, causing oscillations in the Euler characteristic. After the double capillary trapping events, however, the

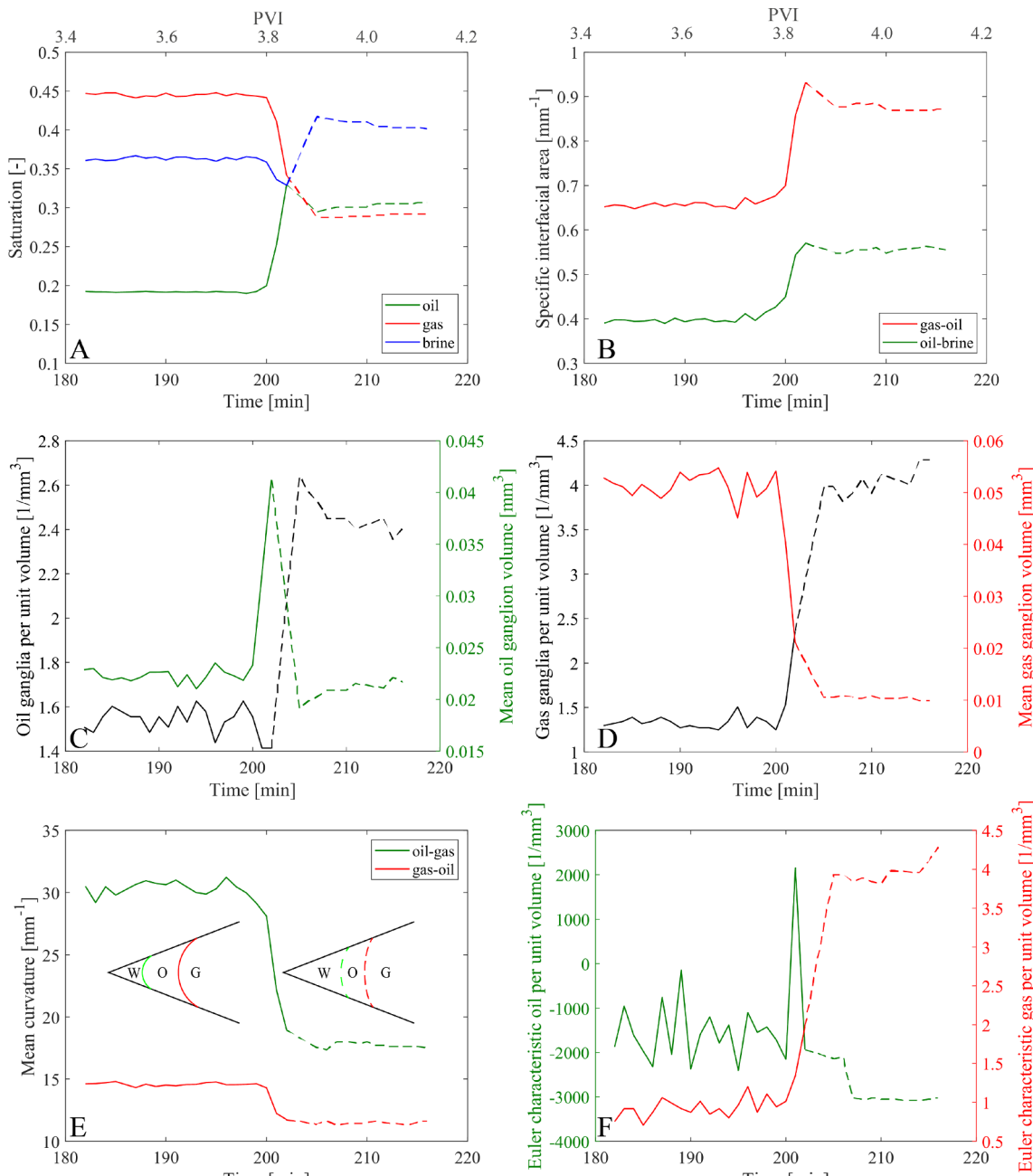


Fig. 7. Minkowski functionals during WF2. A: Saturation of brine (blue), oil (green) and gas (red). B: Gas/oil (red) and oil/brine (green) interfacial areas. C: Number of oil ganglia per unit volume (dark green - left y-axis) and their mean volume (light green - right y-axis). D: Number of gas ganglia per unit volume (dark red - left y-axis) and their mean volume (light red - right y-axis). E: Mean curvature of the oil-brine (green) and gas-oil (red) interfaces. F: Euler characteristic of oil (green) and gas (red) per unit volume. The double trapping events happened between minutes 199 and 206. Before trapping, gas was locally injected (solid line), while later brine invaded the system (dashed line). PVI = pore volumes injected since WF2 started.

oil Euler characteristic was stable as the oil phase was then disconnected and its arrangement did not evolve further over time. In fact, once all the oil and gas were trapped, further brine injection did not alter the fluid arrangement in the pore space. It is interesting though that the oil Euler characteristic decreased after brine injection which is particularly important in the context of enhanced oil recovery where a dispersed but connected phase is more likely to be recovered.

3.3. Remaining gas saturation

The measured initial (S_{gi}) and remaining (S_{gr}) gas saturations of about 45% and 30% at the beginning and end of WF2 respectively, indicate an increase in gas trapping with respect to similar gas-brine

systems. For example, using the Land trapping model, Eq. (1), with the constant $C = 1.73$ found by Al Menhali et al. [31] for a two-phase nitrogen-brine system in a similar carbonate rock, S_{gr} would have been 24%. An increased gas trapping in the presence of oil and brine had been previously observed by other authors [59,15,16]. These results were obtained without using direct fast imaging of the pore space, which instead provides a clear explanation for the enhancement of gas trapping.

Our system was measured to be water-wet. We performed direct contact angle estimation at the end of the first waterflooding using the automatic algorithm developed by Scanziani et al. [47] and we obtained a distribution of contact angles, measured through brine at 1124 brine-oil-solid contact points, with a mean value of $47.5 \pm 4.6^\circ$. The

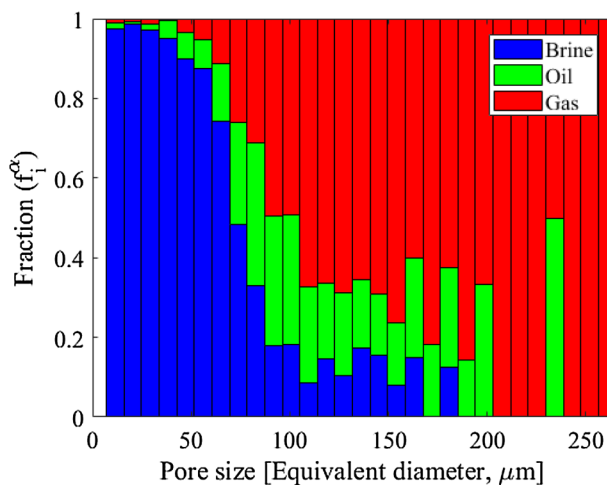


Fig. 8. Pore occupancy for brine, oil and gas at the end of GI.

wettability order in water-wet systems is brine-oil-gas, from the most to the least wetting fluid. This implies that brine occupies the smallest pores, while gas, during gas injection, invaded the biggest ones, as shown in Fig. 8, where pore occupancy is computed at the end of GI.

Secondly, in Section 3.1.1 we described the formation of oil layers. These always surrounded gas (Figs. 5 and 6A-C), thus preventing direct contact between gas, in the largest openings in the pore space, and brine, in the small pores. The stability of oil layers is also proved by Fig. 7E, showing that the mean curvatures always obeyed $\kappa_{ow} > \kappa_{go}$ implying the presence of stable oil layers. The oil layers inhibited direct displacement of gas by brine. Gas was instead contacted by oil which was involved in the double imbibition displacements resulting in double capillary trapping events (Section 3.2). The competition between piston-like displacement and snap-off during these events was then biased towards the latter, as the contact angle between gas and oil is effectively zero [5], due to the presence of oil layers.

As a consequence, at the end of WF2, gas was confined in the centre of the big pores and disconnected in many small ganglia (Figs. 6C,F and 7D), as the positive Euler number confirms (Fig. 7F). This implies secure trapping of gas by capillary and interfacial forces, which would be stable over thousands of years, as for two-phase flow [4,7]. However, the amount of trapped gas in two-phase flow was lower, as the direct contact between gas and brine allowed more piston-like displacement of gas with less snap-off and capillary trapping.

4. Conclusions

Using synchrotron X-ray imaging we dynamically imaged three-phase flow in porous media. Multiple displacements govern the flow during gas injection in a system where oil and brine are present. Both double drainage and double imbibition events were observed, as well as longer chains and combinations of these, called multiple displacements, which had hitherto only been observed in micromodel experiments [20,21]. A chase injection of brine, after gas, caused the gas to be trapped by oil and oil by brine. We name this phenomenon double capillary trapping, which is a particular case of double imbibition where snap-off is favoured over piston-like displacement. This is enabled by the presence of spreading oil layers sandwiched between brine and gas, reducing the effective contact angle between oil and gas to zero, thus favouring gas snap-off. Quantitative measures related to the Minkowski functionals - saturation, interfacial area, mean curvature and Euler characteristic - were used to quantify the fluid topology during the displacement. In particular, the mean curvatures define the capillary pressure during double displacements and confirm the stability of oil layers, while the Euler characteristic quantifies changes in connectivity.

These double capillary trapping phenomena lead to a higher residual gas saturation in three-phase flow compared to an equivalent two-phase oil-water displacement. This shows high potential for carbon dioxide storage at immiscible conditions in depleted oil reservoirs combined potentially with enhanced oil recovery.

Future work should focus on the study of the effects of using CO₂ as the gas phase, with lower gas/oil interfacial tension, approaching miscible conditions. In addition, the study of variable wettability states, would be helpful to increase our knowledge of three-phase flow in porous media, as a change in the wettability order among the three phases can radically change their arrangement in the pore space. The study of three-phase flow, at the pore scale, for different types of rock could also investigate the effects of pore structure, micro-porosity and mineralogy.

Declaration of Competing Interest

The authors declare that they have no known competing financial interests or personal relationships that could have appeared to influence the work reported in this paper.

Acknowledgments

We acknowledge Abu Dhabi National Oil Company (ADNOC) for financial support; Christoph Rau, Shashidhara Marathe, Kaz Wanelik and the staff of Diamond Light Source for their help during the experiments; Qingyang Lin (Imperial College London) for sharing image processing scripts.

Appendix A. Supplementary material

Supplementary data associated with this article can be found, in the online version, at <https://doi.org/10.1016/j.apenergy.2019.114136>.

References

- [1] IEA. 20 Years of Carbon Capture and Storage - Accelerating Future Deployment. International Energy Agency; 2016.
- [2] IEA. Energy Technology Perspectives 2017 - Executive Summary. Tech. rep.; 2017.
- [3] Intergovernmental Panel on Climate Change (IPCC). IPCC Special Report on Carbon Dioxide Capture and Storage; 2005.
- [4] Krevor S, Blunt MJ, Benson SM, Pentland CH, Reynolds C, Al-Mehdhi A, et al. Capillary trapping for geologic carbon dioxide storage – from pore scale physics to field scale implications. *Int J Greenhouse Gas Control* 2015;40:221–37.
- [5] Blunt MJ. Multiphase flow in permeable media. Cambridge University Press; 2017.
- [6] Benson SM, Cole DR. CO₂ sequestration in deep sedimentary formations. *Elements* 2008;4(5):325–31.
- [7] Juanes R, Spiteri EJ, Orr FM, Blunt MJ. Impact of relative permeability hysteresis on geological CO₂ storage. *Water Resour Res* 2006;42(12).
- [8] Burnside N, Naylor M. Review and implications of relative permeability of CO₂/brine systems and residual trapping of CO₂. *Int J Greenhouse Gas Control* 2014;23:1–11.
- [9] Wang X, van 't Veld K, Marcy P, Huzurbazar S, Alvarado V. Economic co-optimization of oil recovery and CO₂ sequestration. *Appl Energy* 2018;222:132–47.
- [10] Ampomah W, Balch RS, Cather M, Will R, Gunda D, Dai Z, et al. Optimum design of CO₂ storage and oil recovery under geological uncertainty. *Appl Energy* 2017;195:80–92.
- [11] Kolster C, Masnadi MS, Krevor S, Mac Dowell N, Brandt AR. CO₂ enhanced oil recovery: a catalyst for gigatonne-scale carbon capture and storage deployment? *Energy Environ Sci* 2017;10(12):2594–608.
- [12] Qi R, LaForce TC, Blunt MJ. Design of carbon dioxide storage in aquifers. *Int J Greenhouse Gas Control* 2009;3(2):195–205.
- [13] Qi R, LaForce TC, Blunt MJ. Design of carbon dioxide storage in oil fields. SPE annual technical conference and exhibition. 2008. p. 21–4.
- [14] Land CS. Calculation of imbibition relative permeability for two- and three-phase flow from rock properties. *Soc Petrol Eng J* 1968;8(02):149–56.
- [15] Amaechi B, Iglesias S, Pentland CH, Bijeljic B, Blunt MJ. An experimental study of three-phase trapping in sand packs. *Transp Porous Media* 2014;103(3):421–36.
- [16] Scanziani A, Singh K, Bultreys T, Bijeljic B, Blunt MJ. In situ characterization of immiscible three-phase flow at the pore scale for a water-wet carbonate rock. *Adv Water Resour* 2018;121:446–55.
- [17] Feali M, Pinczewski WV, Cinar Y, Arns CH, Arns J-Y, South N, et al. Qualitative and quantitative analyses of the three-phase distribution of oil, water, and gas in Bentheimer sandstone by use of micro-CT imaging. *SPE Reserv Eval Eng* 2012;15(January):706–11.

- [18] Oren PE, Billiotte J, Pinczewski WV. Mobilization of waterflood residual oil by gas injection for water-wet conditions. *SPE Format Eval* 1992;7:70–8.
- [19] van Dijke M, Sorbie K. Pore-scale modelling of three-phase flow in mixed-wet porous media: multiple displacement chains. *J Petrol Sci Eng* 2003;39(3–4):201–16.
- [20] Sohrabi M, Tehrani D, Danesh A, Henderson G. Visualization of oil recovery by water-alternating-gas injection using high-pressure micromodels. *SPE J* 2004;9(3):290–301.
- [21] Van Dijke MJ, Sorbie K, Sohrabi M, Danesh A. Three-phase flow WAG processes in mixed-wet porous media: pore-scale network simulations and comparison with water-wet micromodel experiment. *SPE J* 2004;9(1):57–66.
- [22] Keller A, Blunt MJ, Roberts A. Micromodel observation of the role of oil layers in three-phase flow. *Transp Porous Media* 1997;26(3):277–97.
- [23] Fenwick DH, Blunt MJ. Three-dimensional modeling of three phase imbibition and drainage. *Adv Water Resour* 1998;21(2):121–43.
- [24] Blunt MJ, Bijeljic B, Hu D, Gharbi O, Iglauer S, Mostaghimi P, et al. Pore-scale imaging and modelling. *Adv Water Resour* 2013;51:197–216.
- [25] Bultreys T, De Boever W, Cnudde V. Imaging and image-based fluid transport modeling at the pore scale in geological materials: a practical introduction to the current state-of-the-art. *Earth Sci Rev* 2016;155:93–128.
- [26] Singh K, Jung M, Brinkmann M, Seemann R. Capillary-dominated fluid displacement in porous media. *Annu Rev Fluid Mech* 2019;51:429–49.
- [27] Andrew M, Bijeljic B, Blunt MJ. Pore-scale imaging of geological carbon dioxide storage under in situ conditions. *Geophys Res Lett* 2013;40(15):3915–8.
- [28] Andrew M, Bijeljic B, Blunt MJ. Pore-scale imaging of trapped supercritical carbon dioxide in sandstones and carbonates. *Int J Greenhouse Gas Control* 2014;22:1–14.
- [29] Singh K, Bijeljic B, Blunt MJ. Imaging of oil layers, curvature and contact angle in amixed- wet and a water-wet carbonate rock. *Water Resour Res* 2016;52:1–13.
- [30] De Chalender JA, Garing C, Benson SM. Pore-scale modelling of Ostwald ripening. *J Fluid Mech* 2018;835:363–92.
- [31] Al-Mehalli A, Menke H, Blunt MJ, Krevor S. Pore scale observations of trapped CO₂ in mixed-wet carbonate rock: applications to storage in oil fields. *Environ Sci Technol* 2016;50(18):10282–90.
- [32] Iglauer S, Paluszny A, Pentland CH, Blunt MJ. Residual CO₂ imaged with X-ray micro-tomography. *Geophys Res Lett* 2011;38(21).
- [33] Iglauer S, Paluszny A, Blunt MJ. Simultaneous oil recovery and residual gas storage: a pore-level analysis using in situ X-ray micro-tomography. *Fuel* 2013;103:905–14.
- [34] Alhosani A, Scanziani A, Lin Q, Pan Z, Bijeljic B, Blunt MJ. In situ pore-scale analysis of oil recovery during three-phase near-miscible CO₂ injection in a water-wet carbonate rock. *Adv Water Resour* 2019;103432.
- [35] Qin Z, Arshadi M, Piri M. Micro-scale experimental investigations of multiphase flow in oil-wet carbonates. II. Tertiary gas injection and WAG. *Fuel* 2019;257:116012.
- [36] Berg S, Ott H, Klapp SA, Schwing A, Neiteler R, Brussee N, et al. Real-time 3D imaging of Haines jumps in porous media flow. *Proc Natl Acad Sci USA* 2013;110(10):3755–9.
- [37] Andrew M, Menke H, Blunt MJ, Bijeljic B. The imaging of dynamic multiphase fluid flow using synchrotron-based X-ray microtomography at reservoir conditions. *Transp Porous Media* 2015;110(1):1–24.
- [38] Singh K, Menke H, Andrew MG, Lin Q, Rau C, Blunt MJ, et al. Dynamics of snap-off and pore-filling events during two-phase fluid flow in permeable media. *Sci Rep* 2017;7(1):5192.
- [39] Menke HP, Bijeljic B, Andrew MG, Blunt MJ. Dynamic three-dimensional pore-scale imaging of reaction in a carbonate at reservoir conditions. *Environ Sci Technol* 2015;49(7):4407–14.
- [40] Reynolds CA, Andrew M, Menke H, Krevor S, Blunt MJ. Dynamic fluid connectivity during steady-state multiphase flow in a sandstone. *Proc Natl Acad Sci* 2017;114(31):8187–92.
- [41] Rücker M, Bartels W, Singh K, Brussee N, Coorn A, Linde HVD. The effect of mixed wettability on pore scale flow regimes based on a flooding experiment in Ketton limestone. *Geophys Res Lett* 2019;46:3225–34.
- [42] Armstrong RT, McClure JE, Robins V, Liu Z, Arns CH, Schlüter S, et al. Porous media characterization using minkowski functionals: theories, applications and future directions. *Transp Porous Media* 2018;1–31.
- [43] Vogel H-J, Weller U, Schlüter S. Quantification of soil structure based on Minkowski functions. *Comput Geosci* 2010;36(10):1236–45.
- [44] Tanino Y, Blunt MJ. Capillary trapping in sandstones and carbonates: dependence on pore structure. *Water Resour Res* 2012;48(8):1–13.
- [45] Bijeljic B, Raeini AQ, Lin Q, Blunt MJ. Multimodal functions as flow signatures in complex porous media; 2018.
- [46] Niu B, Al-Mehalli A, Krevor SC. The impact of reservoir conditions on the residual trapping of carbon dioxide in Berea sandstone. *Water Resour Res* 2015;51(4):2009–29.
- [47] Scanziani A, Singh K, Blunt MJ, Guadagnini A. Automatic method for estimation of in situ effective contact angle from X-ray micro tomography images of two-phase flow in porous media. *J Colloid Interface Sci* 2017;496:51–9.
- [48] Alhammadi AM, AlRatrou A, Singh K, Bijeljic B, Blunt MJ. In situ characterization of mixed-wettability in a reservoir rock at subsurface conditions. *Sci Rep* 2017;7(1):10753.
- [49] Schlüter S, Sheppard A, Brown K, Wildenschild D. Image processing of multiphase images obtained via X-ray microtomography: a review. *Water Resour Res* 2014(50).
- [50] Wildenschild D, Sheppard A. X-ray imaging and analysis techniques for quantifying pore-scale structure and processes in subsurface porous medium systems. *Adv Water Resour* 2013;51:217–46.
- [51] Hildebrand T, Rüegsegger P. A new method for the model-independent assessment of thickness in three-dimensional images. *J Microsc* 1997;185(1):67–75.
- [52] Lin Q, Bijeljic B, Pini R, Blunt MJ, Krevor S. Imaging and measurement of pore-scale interfacial curvature to determine capillary pressure simultaneously with relative permeability. *Water Resour Res* 2018;54(9):7046–60.
- [53] Legland D, Kiêu K, Devaux M-F. Computation of Minkowski measures on 2D and 3D binary images. *Image Anal Stereol* 2011;26(2):83.
- [54] Raeini AQ, Bijeljic B, Blunt MJ. Generalized network modeling of capillary-dominated two-phase flow. *Phys Rev E* 2018;97:23308.
- [55] Bultreys T, Hoorebeke LV, Cnudde V. Multi-scale, micro-computed tomography-based pore network models to simulate drainage in heterogeneous rocks. *Adv Water Resour* 2015;78:36–49.
- [56] Gao Y, Lin Q, Bijeljic B, Blunt MJ. X-ray microtomography of intermittency in multiphase flow at steady state using a differential imaging method. *Water Resour Res* 2017;53(12):10274–92.
- [57] Rücker M, Berg S, Armstrong RT, Georgiadis A, Ott H, Schwing A, et al. From connected pathway flow to ganglion dynamics. *Geophys Res Lett* 2015;42(10):3888–94.
- [58] Van Dijke MJ, Sorbie KS. Pore-scale network model for three-phase flow in mixed-wet porous media. *Phys Rev E* 2002;66.
- [59] Al Mansoori SK, Iglauer S, Pentland CH, Blunt MJ. Three-phase measurements of oil and gas trapping in sand packs. *Adv Water Resour* 2009;32(10):1535–42.
- [60] National Institute of Standards and Technology. In: Linstrom PJ, Mallard WG, editors. NIST Chemistry WebBook; 2018.